

Sense Me on the Ride: Accurate Mobile Sensing over a LoRa Backscatter Channel

Haotian Jiang, Jiacheng Zhang, Xiuzhen Guo, Yuan He

School of Software and BNRIst, Tsinghua University

{jht19,zhangjc21}@mails.tsinghua.edu.cn,

guoxiuzhen94@gmail.com,heyuan@tsinghua.edu.cn

ABSTRACT

Wireless sensing has great significance in Internet of Things (IoT) applications and has attracted substantial research interests in academia. In this study, we propose Palantir, a first-of-its-kind long-range sensing system based on the LoRa backscatter technology. By utilizing the ON-OFF-Keying modulated backscatter signals, Palantir can perform fine-grained long-range cyclist sensing. Our findings show that sensing is more susceptible to channel quality than communication. Hence, the design of Palantir particularly addresses the critical challenges of signal processing, such as amplitude instability, frequency offset, clock drift, spectrum leakage, and multiplicative noise. We implement Palantir and evaluate its performance by conducting comprehensive benchmark experiments. A prototype is also built and a case study of respiration monitoring in the real world is implemented. Results demonstrate that Palantir can perform accurate sensing at a range up to 100 m, which is twice that of state-of-the-art approaches. The median deviation of the detected motion period is as low as 0.2%.

CCS CONCEPTS

- Human-centered computing → Ubiquitous and mobile computing systems and tools;
- Networks → Cyber-physical networks.

KEYWORDS

LoRa, Backscatter, Sensing

ACM Reference Format:

Haotian Jiang, Jiacheng Zhang, Xiuzhen Guo, Yuan He. 2021. Sense Me on the Ride: Accurate Mobile Sensing over a LoRa Backscatter Channel. In *The 19th ACM Conference on Embedded Networked Sensor Systems (SenSys '21), November 15–17, 2021, Coimbra, Portugal*. ACM, New York, NY, USA, 13 pages. <https://doi.org/10.1145/3485730.3485933>

1 INTRODUCTION

Wireless sensing, which acquires the information of a target by collecting and analyzing wireless signals, is a key enabling technology for ubiquitous Internet of Things (IoT) applications. As more

Xiuzhen Guo is the corresponding author.

Permission to make digital or hard copies of all or part of this work for personal or classroom use is granted without fee provided that copies are not made or distributed for profit or commercial advantage and that copies bear this notice and the full citation on the first page. Copyrights for components of this work owned by others than ACM must be honored. Abstracting with credit is permitted. To copy otherwise, or republish, to post on servers or to redistribute to lists, requires prior specific permission and/or a fee. Request permissions from permissions@acm.org.

SenSys '21, November 15–17, 2021, Coimbra, Portugal

© 2021 Association for Computing Machinery.

ACM ISBN 978-1-4503-9097-2/21/11...\$15.00

<https://doi.org/10.1145/3485730.3485933>

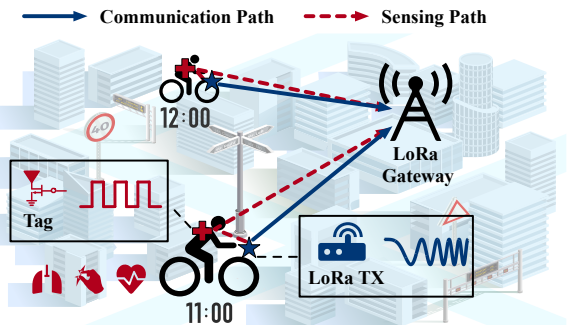


Figure 1: The sketch of cyclist sensing with Palantir.

and more wireless devices are being deployed, knowing how to sufficiently exploit the wireless channels for various sensing purposes has become a crucial and significant problem. In the past decade, we have witnessed a large body of studies on wireless sensing. The wireless technologies for sensing range from acoustic [12, 29, 37], RFID [6, 34, 35, 42, 45] and WiFi [26, 27, 39, 43, 46] to LoRa [3, 41, 48] and mmWave [13], while the sensing capabilities extensively cover motion and activity sensing [6, 19, 28], mobility measurement [42, 45], environmental sensing [35], and material sensing [47], etc.

The aim of our work is to create a new sensing technology for cyclists in the public bicycle sharing systems. Such bicycles are widely used in many countries nowadays. Many of such bicycles are equipped with a long range communication module (e.g. a LoRa transmitter) [5] so that their location data can be uploaded. But how to sense the cyclists' condition, such as the respiration and motions, is still a missing piece in the system.

The sensing technology we invent utilizes the LoRa communication that already exists as the excitation carrier and attaches a simple backscatter tag as the sensor for cyclist sensing, as shown in Figure 1. Such technology is attractive due to the following multi-fold advantages:

First, the sensing range is longer than traditional wireless sensing technologies [12, 35, 39] owing to the long communication range of LoRa. Therefore our proposal can be deployed for outdoor mobile applications.

Second, the sensing cost in terms of hardware and energy is extremely low. What we need to deploy incrementally is merely a backscatter tag. Compared with other options, such as wearable devices (e.g., wristbands) connected with a smartphone [23, 32], our proposal is much more affordable and easy to use.

Third, our proposal utilizes the ambient LoRa transmitter that already exists on the bicycle as the excitation source. Compared to the traditional backscatter technologies that rely on a special

excitation source to function [14], our proposal makes it possible to sense the cyclist on the ride everywhere.

Last but not least, the utilization of the ON-OFF-Keying (OOK) modulated backscatter channel potentially provides fine-grained channel parameters for sensing. Compared with the existing works on LoRa sensing [41, 48], our proposal is most robust against self-interference, channel noise, and the influence of mobility.

To put this idea into practice, however, there is a crucial challenge: *sensing is more susceptible than communication with regard to the channel quality*. An error or noise in the signal, which is usually tolerable in terms of communication, is very likely to hurt the accuracy of the sensing result. Due to the influence of hardware imperfection and complex channel noise, a LoRa backscatter channel in reality falls short of the quality of supporting accurate sensing. In addition, we believe this problem exists not only in LoRa backscatter based sensing but commonly in the combinations of various wireless technologies and their corresponding backscatter systems.

How to retain the accuracy of sensing in the face of the above challenge? In this work, we present Palantir¹, a LoRa backscatter based system for cyclist sensing. Palantir includes a complete signal processing flow to extract high-quality data from the distorted backscatter signals. Specifically, in view of the hardware imperfection, we carefully design a signal shaping method to adjust the signal amplitude and phase and solve the distortion problem caused by spectrum leakage. To deal with complex channel noise, we present an improved clustering algorithm by exploiting the characteristics of additive noise and multiplicative noise. In this way, we can significantly enhance the quality of the backscatter signals and, in turn, increase the sensing range to 100 m. Moreover, we implement Palantir and carry out a case study of respiration monitoring of cyclists to demonstrate the functionalities and effectiveness of Palantir.

To summarize, this paper makes the following contributions:

- We present Palantir, a first-of-its-kind long-range sensing system based on the LoRa backscatter. Palantir extends the sensing range to 100 m, which is twice that of the state-of-the-art LoRa sensing approaches. Palantir can be applied to both stationary and mobile scenarios, thus creating new opportunities for wireless sensing applications.
- We design a complete signal processing flow to particularly deal with multiple challenging problems that are coupled with each other, such as amplitude instability, frequency offset, clock drift, spectrum leakage, and multiplicative noise. Signal quality passing the signal processing flow can meet the high requirements of sensing.
- We evaluate the performance of Palantir by performing comprehensive benchmark experiments. We also build a prototype and conduct a case study of respiration monitoring in the real world. The results demonstrate that Palantir performs accurate sensing at the range of 100 m with a median deviation of motion period to as low as 0.2%.

¹Palantir is a fictional magical artifact from Tolkien's Middle-earth legendarium. A palantir was an indestructible ball of crystal, used for communication and to see events in other parts of the world.

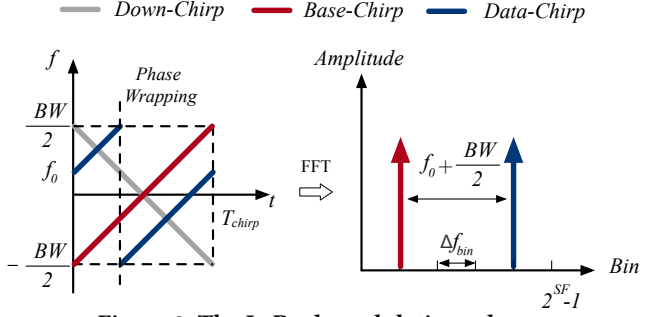


Figure 2: The LoRa demodulation scheme.

Roadmap. The remainder of this paper is organized as follows. In Section 2, we present the communication model and the sensing model, followed by the explanation of the challenges of sensing by using the LoRa backscatter signals. Section 3 presents the design of Palantir. We evaluate the performance of Palantir in Section 4. Section 5 discusses the limitations and potential applications of our proposal. Section 6 surveys related work. We conclude this work in Section 7.

2 SENSING CHANNEL

In this section, we first introduce the communication model of the LoRa backscatter, followed by the theoretical sensing model and the challenges. Our sensing model does not rely on the data modulated by the backscatter tag. At a high level, the basis of Palantir is that the movement of the backscatter tag results in the change of backscatter signal. Thus, the sensing model of Palantir aims to separate the backscatter signal from the received composite signal.

2.1 Communication Model

We first introduce the standard LoRa modulation and demodulation process and then describe the LoRa backscatter based on OOK modulation, which is the basis of our system design.

2.1.1 LoRa primer. LoRa adopts chirp spread spectrum, which enables a long communication range, for modulation. The frequency of chirps changes linearly over time. The LoRa transmitter modulates data on the initial frequency of the chirps. For demodulation, the receiver multiplies an incoming LoRa symbol with a down-chirp and then transforms the multiplication from the time domain to the frequency domain via fast Fourier transform (FFT), yielding a peak on a certain FFT bin. The receiver tracks the location of this peak to demodulate the LoRa symbol accordingly.

We analyze the communication model of LoRa as follows. For each data chirp in LoRa, the frequency increases from an initial frequency f_0 to $\frac{BW}{2}$, wraps to $-\frac{BW}{2}$ and increases back to f_0 . The baseband chirp signal can be represented as:

$$S(t) = e^{j2\pi(f_0t+\frac{1}{2}kt^2)} \quad (1)$$

where k is the frequency change rate. The duration of a single LoRa chirp T_{chirp} is determined on the basis of the spreading factor SF and bandwidth BW :

$$T_{chirp} = \frac{2^S F}{B W} \quad (2)$$

and the frequency change rate k can be represented as:

$$k = \frac{B W}{T_{chirp}} = \frac{B W^2}{2^S F} \quad (3)$$

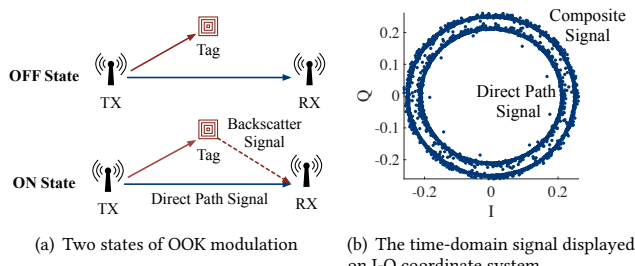


Figure 3: The time-domain signal in the ON and OFF states are distinguishable.

The LoRa data are modulated by applying different f_0 values which fall between $-\frac{BW}{2}$ and $\frac{BW}{2}$.

The LoRa demodulation scheme is shown in Figure 2. To demodulate the receiving signal, the receiver first multiplies an incoming chirp with a down-chirp whose frequency decreases from $\frac{BW}{2}$ to $-\frac{BW}{2}$. A down-chirp can be represented as:

$$S_{down}(t) = e^{j2\pi(\frac{BW}{2}t - \frac{1}{2}kt^2)} \quad (4)$$

After the multiplication, the chirp signal is transformed to a sine wave whose frequency is $f_0 + \frac{BW}{2}$. During demodulation, the receiver applies FFT to this sine wave and tracks the location of the peak on the FFT bin.

In our design, we utilize the standard LoRa demodulation scheme to obtain the start time of the packets and the start frequency f_0 of the chirps. The specific signal model of the LoRa baseband will be further leveraged in our signal processing scheme, which we will explain later.

2.1.2 OOK-based LoRa backscatter. The OOK-based backscatter takes ambient signals as the carrier signal and modulates its data via OOK modulation. In the ON state, the tag reflects the received carrier signal; in the OFF state, the tag absorbs the received carrier signal. As shown in Figure 3, the backscatter signal and the direct path signal form the composite signal at the receiver, and the ON and the OFF states are distinguishable in the time domain. Some existing works, such as Aloba [10], have designed a backscatter proposal to modulate the data on the LoRa chirps using OOK.

To demodulate the OOK signal, we can replace the down-chirp in the standard LoRa demodulation scheme with a *conjugate chirp*², yielding a constant sinusoidal tone. Given the initial frequency f_0 of the incoming chirp, the conjugate chirp is represented as:

$$S'(t) = e^{j2\pi((f_{sin} - f_0)t - \frac{1}{2}kt^2)} \quad (5)$$

Multipled with the conjugate chirp, the received chirp will be transformed to:

$$S(t)S'(t) = e^{j2\pi f_{sin} t} \quad (6)$$

With the knowledge of the boundary time and initial frequency of each chirp, we can eliminate the phase jumping of the sinusoidal tone at the boundary of each chirp and the phase jumping caused by frequency wrapping within the LoRa chirp. Then, the ON and the OFF states can be distinguished by tracking the phase jumping residual in the sinusoidal tone.

²The LoRa chirp and its conjugate chirp are symmetric to each other with respect to the reflection off the X-axis.

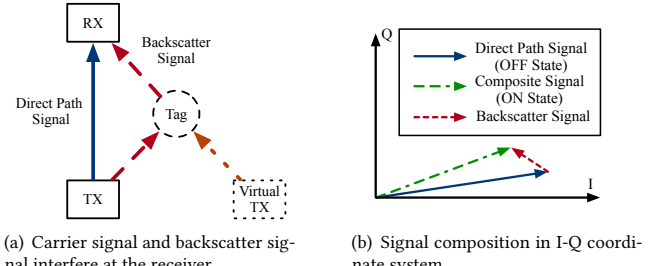


Figure 4: The sensing model based on the interference of carrier signal and backscatter signal.

In this work, we have been inspired to utilize the LoRa backscatter for sensing. The ON state of OOK represents the composite of the direct path signal and the backscatter signal, whereas the OFF state only represents the direct path signal. The OFF state acts as a reference helping to filter out the backscatter signal, which we will explain later.

2.2 Theoretical Sensing Model

In this section, we introduce the theoretical sensing model with the OOK-modulated backscatter. The significance of OOK is that the ON and the OFF states can help to determine the presence or absence of backscatter signals. In previous sensing works, the signal reflected by the target is composed with the line-of-sight signal and other multi-path signals. Thus, multiple antennas are needed to extract the target signal [48]. By contrast, in our proposal, the OFF state acts as a reference. The signal reflected by the backscatter tag can be extracted by subtracting the signal in the ON and the OFF states. This scheme indicates that the backscatter signal can be extracted from the time-domain signal received by a single antenna.

The superposition of the received signal is shown in Figure 4(a). The *Direct path signal* refers to the sub-1 GHz carrier modulated by the LoRa baseband signal, in which the carrier sine wave is referred to as the LoRa carrier. The *backscatter signal* only exists when the backscatter tag is in the ON state, and it is a time-delay version of the direct path signal with an amplitude attenuation. The backscatter tag acts as a virtual transmitter. Therefore, the received signal consists of two interfering signals. The direct path signal can be represented as:

$$S_{ds}(t) = A_{ds}e^{j2\pi f_{lc}t}e^{j2\pi(f_0t + \frac{1}{2}kt^2)} \quad (7)$$

where A_{ds} and f_{lc} are the amplitude of direct path signal and the frequency of the LoRa carrier, respectively. The backscatter signal can be represented as:

$$S_{bs}(t) = A_{bs}e^{j2\pi f_{lc}(t - \frac{d}{c})}e^{j2\pi(f_0(t - \frac{d}{c}) + \frac{1}{2}k(t - \frac{d}{c})^2)} \quad (8)$$

where A_{bs} and c are the amplitude of the backscatter signal and the speed of light, respectively. d represents the difference between the propagation distance of the backscatter signal and that of the direct path signal.

When the backscatter is in the ON state, the received signal is the superposition of S_{ds} and S_{bs} and can be represented as:

$$S_{cs} = S_{ds} + S_{bs} \quad (9)$$

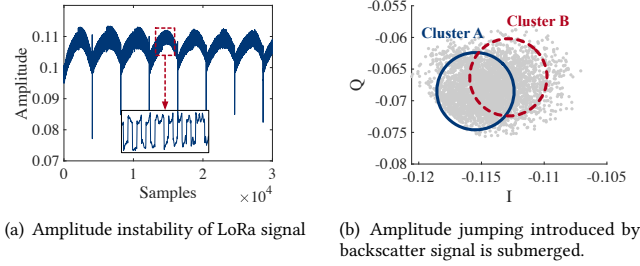


Figure 5: Amplitude jumping introduced by backscatter signal is much smaller than the amplitude instability of LoRa.

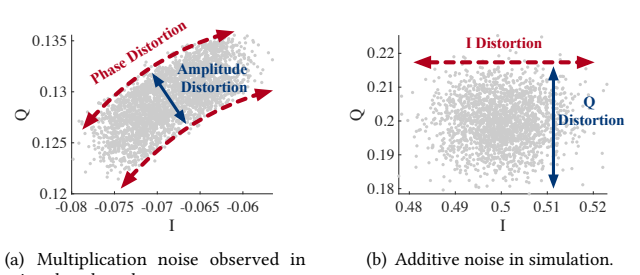


Figure 6: Demonstration of multiplicative and additive noise.

The phase difference of the backscatter signal and the direct path signal can be further represented as:

$$\theta = 2\pi f_{lc} \frac{d}{c} + 2\pi(f_0 \frac{d}{c} + kt \frac{d}{c} - \frac{1}{2}k(\frac{d}{c})^2) \quad (10)$$

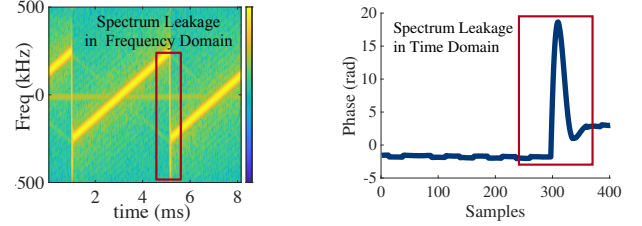
As the LoRa carrier frequency is orders of magnitude larger than the baseband bandwidth, θ can be approximated as:

$$\theta \approx 2\pi f_{lc} \frac{d}{c} \quad (11)$$

When the tag moves relative to the transmitter, the difference of propagation distance (d) also changes. The tag's movement can be determined by calculating the phase difference between the direct path signal S_{ds} and the backscatter signal S_{bs} . Nonetheless, the absolute propagation distance of the backscatter signal is difficult to calculate because θ is wrapped into $[0, 2\pi]$. Fortunately, as long as the tag movement is small between adjacent time windows, we can track the movement of the backscatter tag without ambiguity.

The received signal cannot be used to directly derive d because the signals in the ON and the OFF states never share the same time t in Eq. 7 and Eq. 8. Only if they are transformed into stable signals over time can we accurately calculate the phase difference θ between the backscatter signal and the direct path signal.

In general, the carrier composition $e^{j2\pi f_{lc}t}$ can be removed by the hardware by performing a carrier demodulation. If the LoRa baseband can be further removed, then the stable signal that fits the theoretical model can be derived, as shown in Figure 4(b). However, simply removing the baseband signal is insufficient for sensing. The hardware imperfections and the complex channel noise still remain unresolved, which we will discuss in the following section.



(a) The spectrum of LoRa chirps in micro-benchmark.

(b) Time domain signal after demodulation.

Figure 7: Spectrum leakage in frequency and time domain.

2.3 Challenges of Sensing

In this section, we introduce the specific challenges when utilizing communication signals for sensing in mobile scenarios.

Theoretically, we can remove the LoRa baseband via conjugate multiplication. As represented by Eq. 5, a conjugate chirp transforms the incoming chirp into a constant sinusoidal tone. With $f_{sin} = 0$, the sinusoidal tone can be transformed into a constant signal in the time domain. However, sensing is more susceptible to the channel quality compared with communication. Many factors with a negligible impact on communication can seriously hinder sensing. These factors are the main challenges of sensing, and they can be divided into two categories, namely *hardware imperfections* and *complex channel noise*.

Hardware imperfections exist widely between each pair of transmitters and receivers. We further divide the imperfections into three specific challenges according to the impact, namely amplitude instability, offset and drift, and spectrum leakage. Channel noise is listed separately because we have observed obvious multiplicative noise in the micro-benchmark experiment. The specific challenges can be described as follows:

- 1) **Amplitude Instability.** Although amplitude is not involved in the LoRa modulation scheme, we cannot assume its stability in advance. In the micro-benchmark, the amplitude of the LoRa signal transmitted by a commercial device manifests a visible instability, as shown in Figure 5(a). Figure 5(b) shows the samples in an I-Q coordinate system. The backscatter signal submerges in amplitude instability.
- 2) **Offset and Drift.** Due to hardware imperfections, carrier frequency offset (CFO) and clock drift (CD) always manifest between the transmitter and the receiver. Besides, as the sampling process is discrete, the sample time offset (STO) also has an unpredictable impact on the baseband removal scheme. These offset and drift introduce phase changes over time, which must be resolved to obtain stable signal vectors.
- 3) **Spectrum Leakage.** Spectrum leakage is a common phenomenon in wireless communication. In the case of LoRa, spectrum leakage is especially serious when the chirp frequency jumps, as shown in Figure 7(a). In the time domain, spectrum leakage corresponds to a series of unpredictable signal phases that covers hundreds of samples in the micro-benchmark. As shown in Figure 7(b), a spectrum leakage results in a phase jump after conjugate multiplication.
- 4) **Multiplicative Noise.** In the micro-benchmark, the samples in the I-Q domain form an arc after baseband removal,

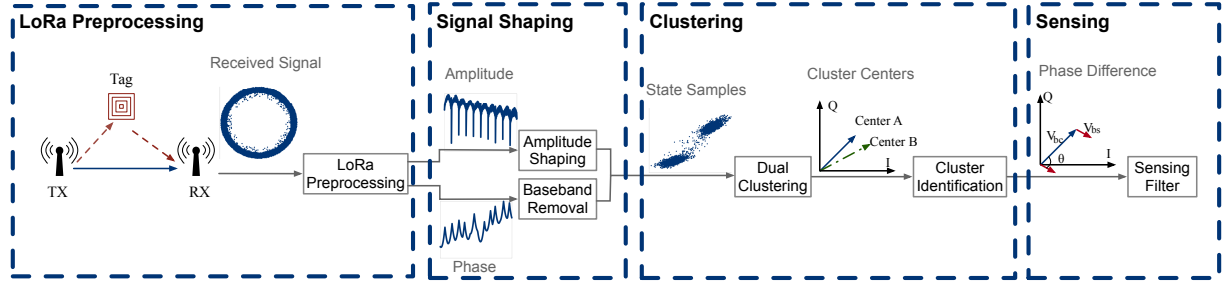


Figure 8: System overview of Palantir.

as shown in Figure 6(a). The presence of an arc cluster indicates that the signal suffers from multiplicative noise instead of additive noise, as the additive noise forms a circular cluster in Figure 6(b). Multiplicative noise is mainly observed because the backscatter tag is close to the transmitter antenna in our scenario. Due to the multiplicative noise, the clustering algorithm based on the Euclidean distance in the I-Q coordinate system is no longer suitable.

All of the aforementioned issues must be carefully resolved before the theoretical sensing model can be used in reality. Unfortunately, the issues are coupled. The phase distortion caused by the spectrum leakage results in a discontinuous signal in the time domain, which further increases the difficulty of solving the other issues. Consequently, we design a complete signal processing scheme to solve the issues.

3 SYSTEM DESIGN

In this section, we introduce the system design of Palantir, as shown in Figure 8. The goal of our design is to transform the received signal into stable signal vectors in the I-Q domain, and calculate the phase difference between the vectors of the direct path signal and the backscatter signal. The design of Palantir is divided into four parts: LoRa preprocessing, signal shaping, clustering, and sensing. The received LoRa signal is demodulated in LoRa preprocessing to generate the initial frequency and the start time of each chirp. Then, the amplitude and phase of the signal are stabilized over time in the signal shaping module. The clustering module clusters those stable signal samples into complex-value clusters whose centers represent the vectors of the direct path signal and the composite signal. With those vectors, the phase difference can be derived, and the movement of the tag can be tracked by the sensing module.

3.1 LoRa Preprocessing

The first step to be implemented after the signal arrives at the receiver is LoRa preprocessing. The LoRa packet is detected and demodulated with a standard LoRa demodulation scheme. Notably, the backscatter signal is orders-of-magnitude weaker than the direct path signal due to the signal attenuation and the insertion loss. This condition allows us to leverage the capture effect and subsequently detect and demodulate the LoRa packet from the direct path signal. This module acts as a necessary preprocessing module, outputting the initial frequency and the start time of each LoRa chirp.

3.2 Signal Shaping

The second step is conducted to transform the received time-domain chirp signal into stable signal samples for clustering. With the aim

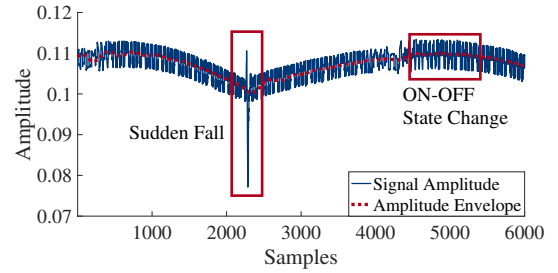


Figure 9: Signal Amplitude. The instability is manifested by amplitude envelopes and sudden fall.

of fitting the model presented in Section 2.2, the samples should be stable in terms of both phase and amplitude, except for the impact of the noise and the state change of backscatter signal. The phase of the received signal changes over time mainly because of LoRa baseband modulation, while the amplitude changes due to the realistic hardware design. As these two reasons are independent from each other, we can separately process the phase and amplitude of the chirp signal.

3.2.1 Amplitude shaping. This module resolves the challenge of **Amplitude Instability**. Amplitude instability impedes the task of distinguishing the clusters representing the ON and the OFF states. Multiple factors lead to amplitude instability, as shown in Figure 9. The first factor is the low-frequency component introduced by the hardware design of the transmitter. The LoRa standard puts no limit on the stability of the signal amplitude, which allows the commercial device to choose its own method of operation. By contrast, the chirp signals generated by the universal software radio peripheral (USRP) have a relatively stable amplitude. The second factor is the sudden fall of the amplitude. This condition is a combined result of the CFO and frequency wrapping. Frequency wrapping from $\frac{BW}{2}$ to $-\frac{BW}{2}$ manifests in each LoRa chirp. Due to the CFO, a part of the highest (or lowest) frequency of the transmitted signal falls beyond the bandwidth of the receiver. As observed in the previous work [25], this condition will result in a sudden fall in amplitude.

In this module, we concentrate on the low-frequency component of the amplitude. The frequency wrapping will be resolved in a later module because it also introduces severe spectrum leakage. It is observed that a high-pass filter distorts the state change of the backscatter signal. Hence, we apply a low-pass filter to derive the amplitude envelope and subtract it from the signal amplitude.

Summary 1: The step of amplitude shaping leverages a low-pass filter to eliminate the amplitude instability caused by hardware

imperfections. This module inputs the amplitude of the received baseband signal and outputs the stable amplitude.

3.2.2 LoRa baseband removal. This module removes the LoRa baseband from the signal phase as resolves the challenge of **Offset and Drift**. Unlike the chirp radar system[7], the sensing with Palantir is based on the carrier signal, which means that the LoRa baseband should be carefully removed. In particular, the main part of the LoRa baseband is removed by conjugate demodulation, i.e., multiplying the chirp signal with the conjugate chirp. A conjugate chirp is represented as Eq. 5, in which $f_{sin} = 0$ and f_0 are calculated in the LoRa preprocessing module. The phase of the received signal and the demodulated signal is shown in Figure 10. However, the signal phase still changes over time after conjugate demodulation. The reason lies in the three kinds of offset and drift. We first separately explain the impact of each type and then eliminate them in a unified manner.

The **CFO** introduces an extra frequency f_{CFO} . The phase of the received signal with CFO can be represented as:

$$\varphi_{CFO}(t) = 2\pi((f_0 + f_{CFO})t + \frac{1}{2}kt^2) \quad (12)$$

We can reasonably assume that the CFO remains the same in a single packet. In general, the CFO will not seriously affect the standard LoRa demodulation. The frequency difference between the neighboring FFT bins is given by:

$$\Delta f_{bin} = \frac{BW}{2SF} \quad (13)$$

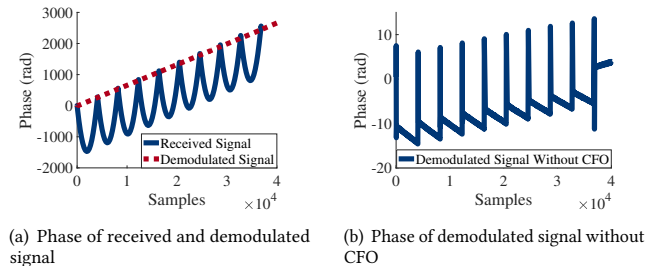
where SF is the spreading factor. This means that a CFO between $-\frac{\Delta f_{bin}}{2}$ and $\frac{\Delta f_{bin}}{2}$ does not change the position of the peak in the FFT bins, and the demodulation results remain correct. For those CFOs with a larger absolute value than $\frac{\Delta f_{bin}}{2}$, each chirp in the same packet has the same offset in the peak of the FFT bin. By aligning the peak of the LoRa preamble, the LoRa can still demodulate correctly while neglecting the small CFO. However, the small CFO must be eliminated because a phase-constant signal is needed.

The **STO** introduces a short time offset Δt in the received signal. Representing the sample rate as F_s , Δt falls between $-\frac{1}{2F_s}$ and $\frac{1}{2F_s}$. As the frequency of the chirp signal changes linearly, the STO introduces a frequency offset $k\Delta t$, which has a much smaller absolute value than $\frac{\Delta f_{bin}}{2}$. Although the STO will not offset the FFT peak, its impact on the phase is maintained after conjugate demodulation. The phase of the received signal with STO can be represented as:

$$\varphi_{STO}(t) = 2\pi(f_0(t + \Delta t) + \frac{1}{2}k(t + \Delta t)^2) \quad (14)$$

Notably, unlike CFO, the STO will introduce a phase jump with the change of f_0 even if the STO is consistent in a single packet. These phase jumps are predictable because we know exactly the change pattern of f_0 . However, the change of f_0 is accompanied by spectrum leakage. Thus, we concentrate on the continuous part of the STO in this section and discuss the phase jumps later.

The **CD** results in a scale factor m on the independent variable t . Taking CD into account, the phase of the received signal can be represented as:



(a) Phase of received and demodulated signal
(b) Phase of demodulated signal without CFO

Figure 10: Phase of the received signal and the demodulated signal. The CFO is the main part of the demodulated signal phase accumulating between chirps, but other factors exist.

$$\varphi_{CD}(t) = 2\pi(f_0mt + \frac{1}{2}k(mt)^2) \quad (15)$$

The CFO, STO or CD does not independently affect the received signal, but they influence each other and eventually change the phase of the received signal to the following:

$$\varphi_{baseband}(t) = 2\pi((f_0 + f_{CFO})m(t + \Delta t) + \frac{1}{2}k(m(t + \Delta t))^2) \quad (16)$$

After conjugate demodulation, the remaining phase caused by these three kinds of offset and drift takes the form of a quadratic polynomial that can be represented as:

$$\begin{aligned} \Delta\varphi_{baseband}(t) &= 2\pi(a_0t^2 + a_1t + a_2) \\ a_0 &= \frac{1}{2}k(m^2 - 1) \\ a_1 &= f_0(m - 1) + f_{CFO}m + \frac{1}{2}km^2\Delta t \\ a_2 &= (f_0 + f_{CFO})m\Delta t + \frac{1}{2}km^2\Delta t^2 \end{aligned} \quad (17)$$

With the constant parameters a_0 , a_1 , and a_2 , we can remove the remaining phase change caused by the offset and drift. Unfortunately, due to spectrum leakage, a_2 is distorted to unpredictable values. Thus, a single packet does not share the same a_2 in its duration, which means that we cannot calculate f_{CFO} , Δt , and m and remove the phase change in the entire packet. However, these parameters can still be calculated in each continuous part of the signal phases via curve fitting as long as the value of f_0 is constant.

Summary 2: This module removes the LoRa baseband from the signal phase and solves the offset and drift problems. We separately analyze the influence of each kind of offset and drift and model their joint impact on the signal phase. This module inputs the phase of the received baseband signal and outputs the stable phases.

3.3 Clustering

Given the previous modules, the received signal can be transformed into signal samples for clustering. The third step of Palantir is clustering, including dual clustering and cluster identification. In particular, we refer to the output of signal shaping as *state samples*. When the backscatter signal stays in the same state (ON/OFF), the state samples are constant in both amplitude and phase except for the impact of noise.

3.3.1 Dual clustering. This module includes **Multiplication Noise** and presents a clustering method that takes both additive noise and multiplicative noise into consideration. The clustering method

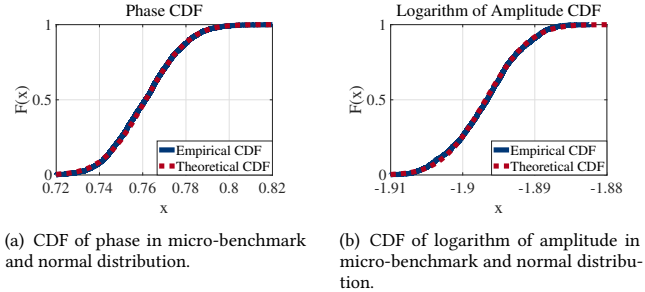


Figure 11: The CDF of phase and logarithm of amplitude, compared with that of normal distribution.

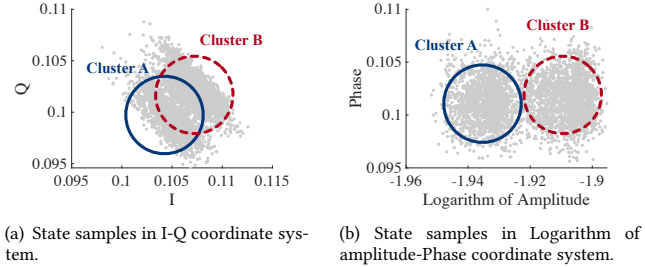


Figure 12: State samples in I-Q and Logarithm of amplitude-Phase coordinate systems.

is based on k-means [15], which is a classic clustering algorithm. As mentioned in Section 2.3, the received signal suffers from multiplication noise and forms an arc in the I-Q coordinate system, which means that simply applying k-means is inappropriate. The clustering method is based on Euclidean distance, which implies that state samples should form a circular cluster. This situation occurs in the I-Q coordinate system only when the additive noise is dominant.

The k-means approach is generally not designed to distinguish arc clusters with multiplicative noise. When two clusters are close to each other, k-means is more likely to cause mistakes in arc clusters than in circular clusters. The state samples can be represented as:

$$S_{sample} = (AA_{noise})e^{j2\pi(\theta+\theta_{noise})} \quad (18)$$

The distortion in the phase of the state samples appears to be additive and follows a normal distribution, and the same situation is true for the logarithm of amplitude, as shown in Figure 11. Hence, the state samples with multiplicative noise form a circular cluster in the logarithm of the amplitude-phase coordinate system, as shown in Figure 12.

Palantir performs k-means in both the I-Q coordinate system and the logarithm of the amplitude-phase coordinate system to deal with additive noise and multiplicative noise, respectively. Normal-distributed distortion equally impacts the state samples in each cluster. Hence, the two clusters generated by k-means should have similar standard deviations, which can be used to judge the accuracy of clustering. If the clustering results in both coordinate systems are accurate, then they vote to decide the result of dual clustering. This scenario means that some state samples in the transition zone are abandoned, which is conducive to improving the estimation of the cluster centers. However, if one of the clustering results is

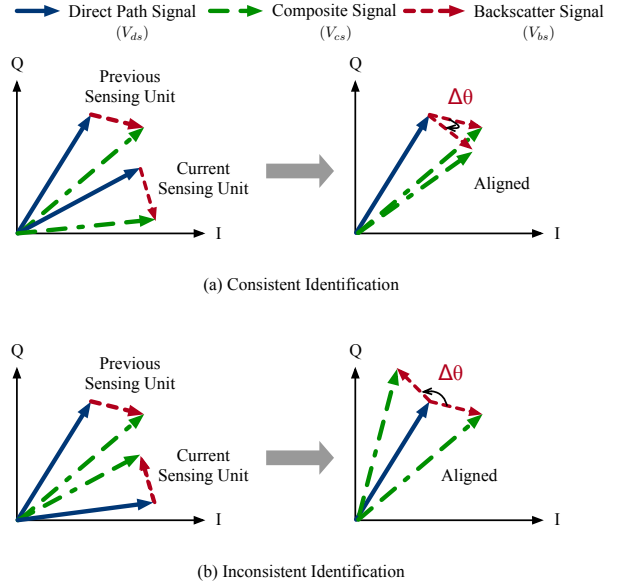


Figure 13: Inconsistent identification results in a large $\Delta\theta$, which represents an abnormal velocity. In order to compare $\Delta\theta$ in (a) and (b), we rotate to align V_{ds} .

relatively inaccurate, then either multiplicative noise or additive noise is dominant. We simply ignore the inaccurate one and output the better clustering result.

Summary 3: This module focuses on multiplicative noise. By transferring the state samples from the I-Q coordinate system to the logarithm of the amplitude-phase coordinate system, we can transform the arc clusters into circular clusters. Moreover, the dual clustering scheme takes both additive noise and multiplicative noise into consideration. The input of this module is the state samples, and the output is the centers of clusters.

3.3.2 Cluster identification. This module resolves the challenge of **Spectrum Leakage**. Although samples in the time domain can be clustered, it is nontrivial to identify the ON and the OFF states. Without extra knowledge of encoding, it is impossible to directly identify which state each of the cluster represents. In this section, we first prove that as long as the identification is consistent, a mismatch of the ON and OFF states does not harm the sensing result. Thereafter, we present a method to guarantee the consistency.

After stabilization, the signal samples can be clustered into complex-value cluster centers. We use the complex signal vectors V_{ds} , V_{bs} , and V_{cs} to represent the direct path signal, backscatter signal, and composite signal, respectively. For the sensing task, knowing exactly which cluster a sample is located is unnecessary. The focus are the centers of the clusters, as they represent signal vectors V_{ds} and V_{cs} . The spectrum leakage introduces a series of unpredictable signal phases, which breaks an entire packet into pieces of samples with continuous phases. We refer to these pieces as maximum sensing units. The backscatter tag is regarded to be motionless in a single sensing unit. For fine-grained sensing, a smaller sensing unit can be chosen as long as the backscatter signals in both the ON and OFF states exist in each unit.

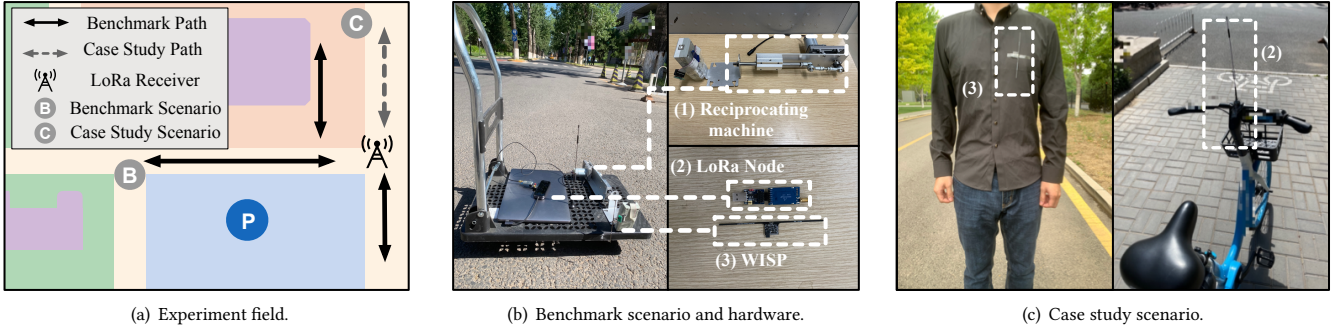


Figure 14: Experimental setup. (1) Reciprocating machine. (2) LoRa Node. (3) WISP.

Hundreds of samples must be abandoned when the frequency jumps. Even more problematic, the phase jumps because of the STO when the frequency jumps, as mentioned in Section 3.2.2. This means that the movement of the backscatter tag cannot be represented by the phase of the signal vector V_{bs} . To determine the tag movement between adjacent sensing units, we calculate the change in angle between V_{ds} and V_{bs} , which can be represented as :

$$\Delta\theta = \ln \frac{V_{bs2}}{V_{ds2}} - \ln \frac{V_{bs1}}{V_{ds1}} = \ln \frac{V_{bs2}}{V_{bs1}} \frac{V_{ds1}}{V_{ds2}} \quad (19)$$

V_{ds} and V_{cs} does not have an equal role in the sensing model. In the presence of $V_{bs} = V_{cs} - V_{ds}$, if we mismatch the cluster centers and the states, then the above equation will turn into:

$$\Delta\theta' = \ln \frac{-V_{bs2}}{V_{bs2} + V_{ds2}} - \ln \frac{-V_{bs1}}{V_{bs1} + V_{ds1}} = \ln \frac{V_{bs2}}{V_{bs1}} \frac{V_{bs1} + V_{ds1}}{V_{bs2} + V_{ds2}} \quad (20)$$

Notably, the magnitude of V_{ds} is orders-of-magnitude larger than that of V_{bs} . We regard V_{ds} as a constant among adjacent sensing units, i.e., $\Delta\theta \approx \Delta\theta'$. Therefore, there will be no effect even if we mistake all V_{ds} for V_{cs} and all V_{cs} for V_{bs} at the same time.

In ensuring the consistency of the identification, we can reasonably assume that the tag movement between the adjacent sensing units is small. As shown in Figure 13, an inconsistent identification causes a large $\Delta\theta$ between adjacent sensing units, i.e., an abnormal velocity. Hence, we choose the identification with a smaller $\Delta\theta$ to ensure consistency.

Summary 4: This module resolves the last challenge of spectrum leakage. We have proven that a global mismatch will not harm the sensing result as long as the identification is consistent. Consistency is ensured by assuming that the tag movement is small in a relatively short time. This module takes the cluster centers as the input, classifies them according to ON and OFF states, and outputs the phase changes caused by the tag movement between the adjacent sensing units.

3.4 Sensing

The final step of Palantir is sensing. We have calculated $\Delta\theta$ between adjacent sensing units. The change of flying distance of backscatter signal can be calculated as:

$$\Delta d = \frac{c\Delta\theta}{2\pi f_{lc}} \quad (21)$$

When the tag crosses the line-of-sight path between the transmitter and the receiver, the mirror position may pose a problem [4].

This issue results in an ambiguity in the moving direction, but the ambiguity can be identified on the basis of the sudden change in the tag's speed. Hence, the impact of mirror position can be eliminated.

For certain applications, some optional improvements will still remain. For example, respiration sensing can attain better results by applying a band-pass filter. Particularly, in mobile scenarios in which the transmitter is moving, a high-pass filter may be necessary. This condition can be attributed to the movements of the transmitter that change the propagation distance of the direct path signal, which means V_{ds} rotates inherently. As the calculation of Δd is based on the angle between V_{ds} and V_{bs} , the rotation of V_{ds} is passed on to Δd . This restriction hinders complete and accurate tracking with a moving transmitter but has no influence on frequency sensing, such as respiration monitoring.

Summary 5: This module is the final step of sensing, transforming the phase changes back into the changes in propagation distance Δd . As the final output of Palantir, Δd can be further used for certain sensing applications.

4 EVALUATION

In this section, we conduct comprehensive experiments to study the performance of Palantir in various situations. In Section 4.1, we will introduce the hardware and experimental settings. In Section 4.2, we will quantitatively evaluate the performance of Palantir by using a reciprocating machine that generates stable and controllable movements. In Section 4.3, we will measure the respiration of a volunteer while riding a bicycle.

4.1 Experimental Setup

Our experimental setup is shown in Figure 14. We take a commercial LoRa node (a Semtech SX1276 chip) as our transmitter and a USRP N210 as the receiver. Both the transmitter and the receiver are equipped with an omni-directional antenna. The LoRa node runs at 902 MHz with $SF = 11$ and $BW = 500$ KHz. In general, BW and SF determine the LoRa communication range but do not influence the sensing result because the signal strength in the time-domain does not change with BW and SF . The USRP is placed at a fixed position on the road and samples at 1 MHz. A WISP 5.0 is used as the backscatter tag which is powered by a battery. The energy cost of Palantir is the same as that in Aloba[10], which is 0.3 mW. In the benchmark experiments, a reciprocating machine is used to generate a controllable periodic motion. Given the size of the reciprocating machine, it cannot be installed on a bicycle. For

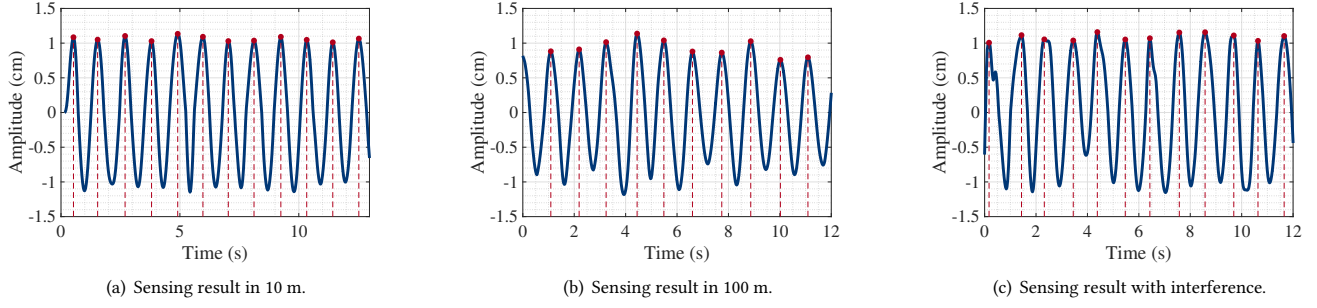


Figure 15: Sensing result in 10 m, 100 m and under interference.

benchmarking in mobile scenarios, we use a trolley as an alternative. Palantir senses the motion period and the motion amplitude of the tag to determine how fast and how deep the breath is, respectively. We rely on the deviation of the sensed period and amplitude to evaluate the performance of Palantir.

4.2 Benchmark Experiments

We conduct comprehensive experiments to evaluate the sensing accuracy of Palantir by using two metrics, i.e., *motion period deviation* and *motion amplitude deviation*. The motion period deviation is calculated by extracting an effective peak in the sensing result, and then the time interval between adjacent peaks is treated as a period. This method results in a higher standard deviation compared with revolutions per minute (RPM), but the fine-grained sensing quality is also revealed. As for the motion amplitude deviation, we treat the peak-to-valley difference in a period as a motion amplitude sample. Figure 15 shows the sensing result in 10 m and 100 m, and a case of interference in which a volunteer moves around. The period is marked with red lines. Palantir performs accurate sensing at a distance of 10 m. The sensing results have a high accuracy in the motion period.

4.2.1 Impact of TX-RX distance. We conduct our experiments in different TX-RX distances to evaluate the sensing range of Palantir. Figure 16 shows the relative error of the motion period and motion amplitude when the TX-RX distance is 10 m, 20 m, 30 m, 40 m, 50 m, and 100 m. The motion period deviation when the TX-RX distance is 10 m has a median of 0.3%, and the ground-truth motion frequency is 1 Hz. As the distance between TX and RX widens, the motion period deviation has a larger range, which means that the sensing accuracy of a single period decreases. The maximum motion period deviation can reach 5% when the TX-RX distance is 100 m, while the median deviation remains small (-0.2%). However, the motion amplitude deviation increases with TX-RX distance from 4.39% at 10 m to 11.65% at 100 m. This trend can be attributed to the decrease in signal noise ratio (SNR) with a longer propagation distance due to the signal attenuation. As mentioned in Section 3.3, in obtaining accurate sensing results, the position of the cluster center must be carefully detected. A lower SNR may result in a larger radius of clusters, causing a partial overlap of the different clusters. This condition can adversely affect the accuracy of the cluster centers and ultimately lead to a decrease in accuracy of the motion amplitude. Nevertheless, Palantir can complete the accurate sensing tasks at a distance of 100 m.

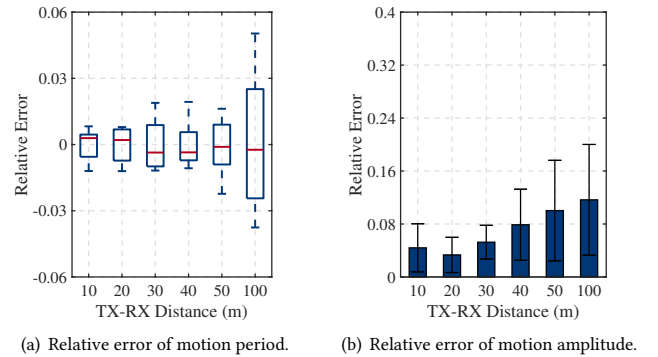
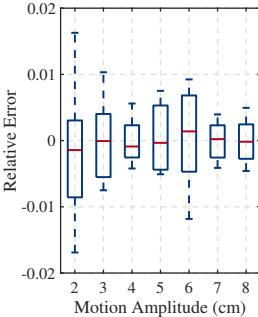


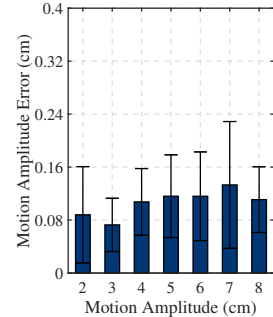
Figure 16: Impact of TX-RX distance.

4.2.2 Impact of motion amplitude. We conduct our experiments with different motion amplitudes to evaluate whether Palantir can be applied to different sensing scenarios. The ground-truth of motion amplitude is obtained according to the reciprocating machine's settings. The statistical results are shown in Figure 17. As the ground-truth motion distance is shown in X-axis, we plot the *absolute deviation* of the motion amplitude instead of the relative error in Figure 17(b). We select seven different motion amplitudes between 2 cm and 8 cm. The period deviations are low in all settings, but they are even slightly lower when the motion amplitude is long. This finding may be explained by the change in amplitude which is steeper with the same frequency and a longer motion amplitude. Compared with a flatter amplitude change pattern, the steeper pattern further clarifies the peak position. However, the absolute deviation of the sensed motion amplitude does not show variations among the different settings. This result means that Palantir can work sufficiently with different motion amplitudes, and it can fit the need of different sensing scenarios.

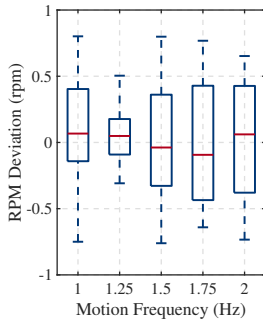
4.2.3 Impact of motion frequency. We also evaluate Palantir with different motion frequencies. The statistical results are shown in Figure 18. Similar to the setting described above, as the different ground-truth values are shown in X-axis, we replace the relative error of motion period in 17(a) with RPM deviation. Notably, the RPM sample is obtained via a simple division with the time of each period, and the results show a larger standard deviation compared with the results of long-term statistics. The experiments in all settings show a median deviation of lower than 0.1 RPM. As mentioned previously, a steeper amplitude pattern means that the movement near the extreme point is faster. This can explain why



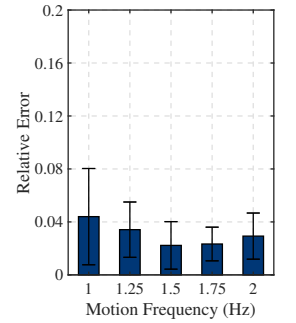
(a) Relative error of motion period.



(b) Motion amplitude deviation.

Figure 17: Impact of motion amplitude

(a) RPM deviation.



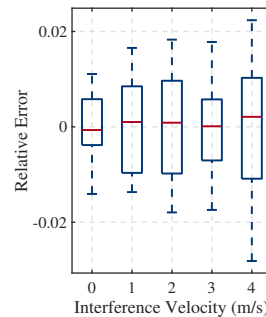
(b) Relative error of motion amplitude.

Figure 18: Impact of motion frequency.

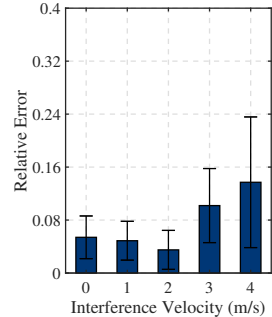
the relative error of motion amplitude is slightly smaller with a higher motion frequency. This benefit is observed in the RPM deviation because a higher frequency indicates that the same period deviation is transformed into a higher RPM deviation.

4.2.4 Impact of Interference. The experiments have been conducted to evaluate the impact of interference on Palantir. Previous works in wireless sensing have shown strong sensitivity to interference. A good explanation is that the interference sources do not differ from the sensing target in signal reflection patterns. Palantir leverages the OOK backscatter to generate a distinguishable signal in the time domain, enabling the sensing target to stand out from the interference. Thus, the interference is treated as an environmental reflection. To evaluate the impact of interference, the volunteer is instructed to move at different speeds around the propagation path. The statistical results are shown in Figure 19. When the volunteer moves at 4 m/s, the motion period deviation ranges from -2.8% to 2.2%, and the median relative error of motion amplitude can reach 13.7%. The movement of the interference source may have different impacts on the TX-RX path and the backscatter path. According to the signal propagation model, the signal attenuates quickly after multiple reflections. This scenario means that a reflector is not likely to introduce multi-path interference to the backscatter signal but only to the direct path signal. Thus, the decrease in sensing accuracy can be mainly attributed to the decrease in SNR when the line-of-sight path is blocked by the interference.

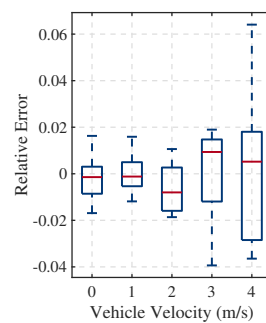
4.2.5 Impact of vehicle velocity. Finally, we evaluate the performance of Palantir in the mobile scenario. The statistical results are



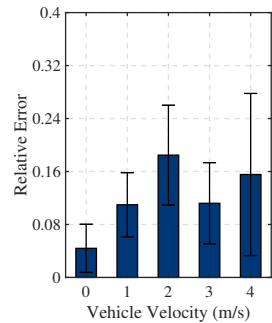
(a) Relative error of motion period.



(b) Relative error of motion amplitude.

Figure 19: Impact of interference velocity.

(a) Relative error of motion period.



(b) Relative error of motion amplitude.

Figure 20: Impact of vehicle velocity.

shown in Figure 20. As mentioned previously, the movement of a vehicle can be removed by using a high-pass filter. However, the filtering method due to its imperfection, inherently decreases the accuracy of the motion amplitude. The period deviations when the trolley moves at 3 and 4 m/s are high mainly due to the bumps caused by uneven roads. These bumps cause the transmitter and tag to experience jitters in different patterns, which distorts the motion period of the backscatter tag. This distortion is extremely strong along rugged roads and if vehicles do not have shock absorbers, such as a trolley. Fortunately, bicycles, wheelchairs, and strollers are more resistant to bumps than trolleys owing to their shock absorbers and inflatable wheels. Nevertheless, Palantir keeps the median of the amplitude deviation to as low as 16%.

4.3 Case Study

With the development of IoT and LoRaWAN, the coverage of LoRa gateways has also widened. Owing to its long communication range and low power consumption, LoRa can be well applied to the public bicycle sharing system. The LoRa transmitter node is usually cheap and portable and hence can be widely installed on vehicles such as bicycles. This case study on Palantir provides an example of outdoor long-term continuous monitoring. Our study, including the experiments, has been approved by the Institutional Review Board. The experiments and results can be summarized as follows:

Experiments: Our case study is about respiration sensing while riding a bicycle. As shown in Figure 14(c), we attach the omnidirectional antenna to the public bicycle. The WISP 5.0 is attached onto the clothes on the chest. The respiration of a volunteer is

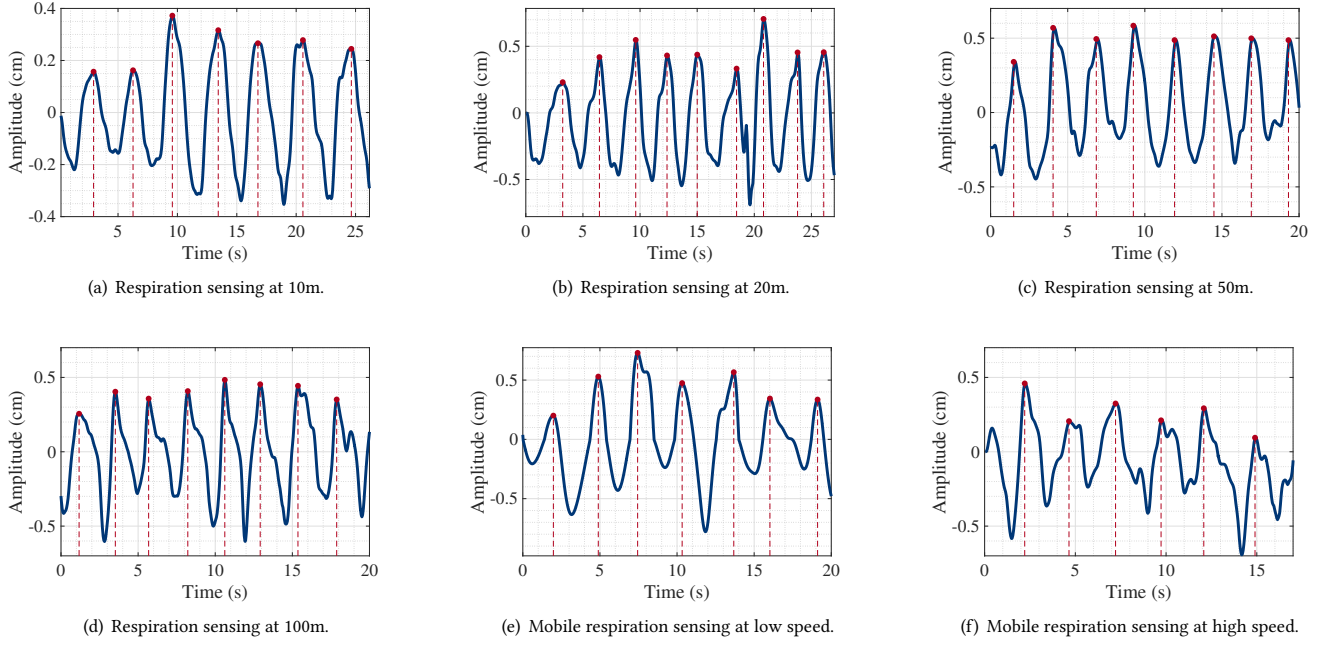


Figure 21: Case study: Respiration sensing at different distance and speed.

sensed at the distance of 10, 20, 50, and 100 m. Then, the volunteer is instructed to ride the bicycle at slow and high speeds, i.e., average speed of 3 and 5 m/s, respectively. Our case study has been designed to verify the feasibility of the proposed scheme in the actual scene. Thus, the ground truth of respiration is not collected.

Results: The sensing results are shown in Figure 21. The red dotted lines mark the respiratory period detected by Palantir. Palantir obtains stable periodic changes, which can be used as a clue for respiration monitoring, as shown in Figure 21(a). As the propagation distance increases, the SNR gradually decreases, which leads to a slight decrease in the stability of the sensing results. As shown in Figure 21(b)-(d), some jitters with small amplitude have appeared, but accurate sensing results can still be obtained. Furthermore, as shown in Figure 21(e)-(f), more jitters appear in the sensing result when the speed increases. This finding can be attributed to the bumps caused by uneven roads. Nevertheless, Palantir can perform accurate respiration sensing in mobile scenarios.

5 DISCUSSION

Sensing Range. Palantir can achieve sensing in hundreds of meters with an OOK backscatter, indicating that the number of receivers can be significantly reduced. Unfortunately, when the tag moves to the middle of the transmitter and the receiver, the signal attenuation reaches its peak [33]. Theoretically, this scenario not only happens when the backscatter tag acts as a reflector, but it also exists widely in the reflection process of wireless signal. Previous works [41, 48] use panel antennas to generate stronger signals. However, in mobile scenarios, panel antennas are not an available option because the tag-to-antenna direction changes in a large range. Moreover, panel antennas are not easy to install or carry on small vehicles, such as bicycles. With omni-directional antennas, the backscatter tag should be no more than meters away from the transmitter (or

receiver), while the distance between the transmitter and the receiver can be in hundreds of meters. We believe this limitation is acceptable because a LoRa transmitter is cheap and small, and LoRa gateways are deployed sparsely with power supplies.

Application Scenarios. The bicycle-sharing system is an application scenario of Palantir. A public bicycle rental authority may want to use the respiration data to improve bicycle design or provide emergency assistance. The current wearable motion sensors usually have a short communication distance, and the sensing data must be transferred via smartphones and cellular networks. By contrast, Palantir supports direct information collection. Moreover, with the aim of alleviating potential privacy concerns, the collected data can be associated with each bicycle instead of the cyclist.

Multi-User Scenarios. The multi-user scenarios are diverse, and they depend on the different combinations of transmitters and tags. Palantir can deal with a scenario in which multiple tags are attached to a cyclist [10] and a scenario involving multiple transmitters and a single tag [36]. Moreover, the sensing accuracy will increase with a higher transmission rate of the LoRa node. This means that the signals from multiple users are more likely to collide in air. Orthogonal parametric settings and channel hopping may be good options in handling signal collisions in multi-user scenarios.

Benefits of Multi-Antenna. A multi-antenna design may enhance the performance of Palantir; this aspect is planned in our future work. If multi-antennas can be designed to independently operate Palantir, then errors can be reduced with the averaging of measurement data. On the other hand, as the angle of arrival of the signals can be calculated, Palantir can also obtain an additional dimension of information.

Doppler Effect. As our sensing target is mobile, a concern may be whether the Doppler effect will be a problem. According to Eq. 11, the impact of the Doppler effect is negligible in Palantir, because

the speed of a bicycle is orders of magnitude lower than that of the electromagnetic wave.

6 RELATED WORK

Our work is related to the following three research areas:

6.1 Backscatter Sensing

The idea of utilizing the backscatter system for sensing has been proposed for a long time. RFID, as the representative technology, has been widely employed for sensing. TagBeat [45] inspects micro and high-frequency mechanical vibrations with commercial off-the-shelf RFID tags and readers. TagSMM [42] presents a RFID-based vibration sensing system which can measure vibration amplitude in sub-millimeter resolution. RFree-GR [6] achieves complex and fine-grained gesture recognition with a Multimodal Convolutional Neural Network. Despite the continuous development of RFID sensing, the limitation of the sensing range has not been solved. The symmetrical design of COTS reader makes the RFID tags always at the midpoint of the propagation path, which corresponds to the most serious attenuation and makes it easy to submerge in the self-interference. To extend the sensing range, the researchers turn their attention to other backscatter systems.

6.2 LoRa Backscatter

Recently, LoRa has attracted significant attention owing to its long communication range and low energy consumption. Various applications, such as smart agriculture [38], smart home [22] and emergency rescue [2] utilize LoRa as the communication method. However, as evaluated in previous works [20, 21], the scalability of LoRa is limited due to its long channel occupation. Some works [8, 17] have attempted to avoid signal collisions by designing efficient MAC layer protocols, while others sought other techniques in solving this problem through parallel decoding [31, 36, 40].

Contrary to the above scheme, some researchers changed their perspective towards superimposed signals. The backscatter system, which has been applied to a wide range of RF signals [14, 44] and is limited by communication distance, happens to fit the need of LoRa. LoRa Backscatter [30] can reach a communication distance of 2.8km when co-located with an RF-source by synthesizing legitimate LoRa packets. PLora [24] takes an ambient LoRa signal as the excitation signal, thus modulating the original chirp into a new standard LoRa chirp signal on a different LoRa channel. XORLora [18] can achieve backscatter communication with commodity LoRa devices through frequency shifting. However, PLoRa and XORLora have a low spectrum efficiencies due to the frequency shifting. Aloba[10], which is the most relevant work with respect to Palantir, applies the OOK modulation to the LoRa backscatter system. This development has inspired us to design a side-channel sensing scheme for long-distance scenarios.

6.3 LoRa-based Sensing

Besides communication, LoRa has also attracted many researchers in other applications. Various works have focused on indoor and outdoor localizations with LoRa [1, 9, 11, 16]. In recent years, several works have leveraged the advantages of LoRa's communication range to realize long-distance sensing. WideSee [3] can realize

wide-area human sensing with a directional antenna. However, only large-scale human activities, such as walking or waving hands, can be sensed by WideSee due to its coarse resolution. In view of achieving a much larger coverage, a drone can be utilized to carry the LoRa transceiver pair and its control system.

The work of Zhang et al. [48] is another development for LoRa sensing, as their research has utilized multiple antennas at the receiver side to extract the reflected signal. Their work increases the sensing range to 25 m for human respiration sensing. However, a longer sensing range means more interference. All moving targets in the sensing range are sensed by the LoRa signal, which means the target of interest cannot be easily distinguished. Sen-fence [41] allows for improvements on this basis. Through software-level beamforming, Sen-fence narrows the sensing to a beam-shaped area. With multiple receivers, Sen-fence forms a closed sensing area and weakens the interference outside the area, achieving a sensing range of 50 m. However, although Sen-fence can reduce interference, it also introduces new restrictions. The sensing area needs to be taken as prior knowledge, and multiple antennas and multiple receivers are needed. Most importantly, this solution can hinder the sensing of large-scale activity and the sensing in mobile scenarios.

Summary: Our work, Palantir, takes advantage of the LoRa and backscatter technology in sensing. By applying the OOK-modulated backscatter to LoRa sensing, Palantir not only can achieve a sensing range of 100 m but also works sufficiently in mobile scenarios. On basis of the existing works on LoRa backscatter [10], Palantir can explore the potential sensing ability of existing communication channels. Compared with the existing sensing works, our research on Palantir no longer requires an accurate prior knowledge of the target location (or initial location), thus expanding the application scenarios of long-range wireless sensing. To the best of our knowledge, Palantir is the first work of its kind that achieves wireless sensing of fine-grained behaviors (e.g., respiration) for long-range mobile targets.

7 CONCLUSION

In this work, we propose Palantir, a sensing system based on the LoRa backscatter. Palantir not only can achieve long-range sensing but is also applicable to mobile scenarios. We reveal the gap between sensing and communication and design a practical signal processing scheme to extract stable signals for sensing with a single-antenna receiver. Although we design Palantir based on the LoRa backscatter, our work fills the gaps between sensing and communication that commonly exist in all kinds of wireless signals. With Palantir, the sensing range can be increased to 100 m, which is twice the range of state-of-the-art work. Palantir also works sufficiently for sensing mobile targets, providing an example for long-term ubiquitous sensing with public bicycles.

ACKNOWLEDGMENT

We thank our shepherd and the anonymous reviewers for their insightful comments. This work is supported in part by National Key R&D Program of China No. 2017YFB1003000, National Science Fund of China under grant No. 61772306, and the R&D Project of Key Core Technology and Generic Technology in Shanxi Province (2020XXX007).

REFERENCES

- [1] A. Bansal, A. Gadre, V. Singh, A. Rowe, B. Iannucci, and S. Kumar. Owl: Accurate lora localization using the tv whitespaces. In *IPSN*. ACM/IEEE, 2021.
- [2] G. M. Bianco, R. Giuliano, G. Marocco, F. Mazzenga, and A. Mejia-Aguilar. Lora system for search and rescue: Path-loss models and procedures in mountain scenarios. *IEEE Internet of Things Journal*, 8(3):1985–1999, 2020.
- [3] L. Chen, J. Xiong, X. Chen, S. I. Lee, K. Chen, D. Han, D. Fang, Z. Tang, and Z. Wang. Widesee: Towards wide-area contactless wireless sensing. In *SenSys*. ACM, 2019.
- [4] Z. Chen, P. Yang, J. Xiong, Y. Feng, and X.-Y. Li. Tagray: Contactless sensing and tracking of mobile objects using cots rfid devices. In *INFOCOM*. IEEE, 2020.
- [5] D. Croce, D. Garlisi, F. Giuliano, A. L. Valvo, S. Mangione, and I. Tinnirello. Performance of lora for bike-sharing systems. In *AEIT AUTOMOTIVE*, 2019.
- [6] C. Dian, D. Wang, Q. Zhang, R. Zhao, and Y. Yu. Towards domain-independent complex and fine-grained gesture recognition with rfid. *Proceedings of the ACM on Human-Computer Interaction*, 4(SIG):1–22, 2020.
- [7] R. J. Fitzgerald. Effects of range-doppler coupling on chirp radar tracking accuracy. *IEEE Transactions on Aerospace and Electronic Systems*, AES-10(4):528–532, 1974.
- [8] A. Gamage, J. C. Liando, C. Gu, R. Tan, and M. Li. Lmac: Efficient carrier-sense multiple access for lora. In *MobiCom*. ACM, 2020.
- [9] C. Gu, L. Jiang, and R. Tan. Lora-based localization: Opportunities and challenges. In *EWSN*. ACM, 2019.
- [10] X. Guo, L. Shangguan, Y. He, J. Zhang, H. Jiang, A. A. Siddiqi, and Y. Liu. Aloba: rethinking on-off keying modulation for ambient lora backscatter. In *SenSys*. ACM, 2020.
- [11] G. Y. Ha, S. B. Seo, H. S. Oh, and W. S. Jeon. Lora toa-based localization using fingerprint method. In *ICTC*. IEEE, 2019.
- [12] J. Han, A. J. Chung, M. K. Sinha, M. Harishankar, S. Pan, H. Y. Noh, P. Zhang, and P. Tague. Do you feel what i hear? enabling autonomous iot device pairing using different sensor types. In *SP*. IEEE, 2018.
- [13] C. Jiang, J. Guo, Y. He, M. Jin, S. Li, and Y. Liu. mmvib: micrometer-level vibration measurement with mmwave radar. In *MobiCom*. ACM, 2020.
- [14] B. Kellogg, V. Talla, S. Gollakota, and J. R. Smith. Passive wi-fi: Bringing low power to wi-fi transmissions. In *NSDI*. USENIX, 2016.
- [15] K. Krishna and M. N. Murty. Genetic k-means algorithm. *IEEE Transactions on Systems, Man, and Cybernetics, Part B (Cybernetics)*, 29(3):433–439, 1999.
- [16] K.-H. Lam, C.-C. Cheung, and W.-C. Lee. Rssi-based lora localization systems for large-scale indoor and outdoor environments. *IEEE Transactions on Vehicular Technology*, 68(12):11778–11791, 2019.
- [17] L. Leonardi, F. Battaglia, and L. L. Bello. Rt-lora: A medium access strategy to support real-time flows over lora-based networks for industrial iot applications. *IEEE Internet of Things Journal*, 6(6):10812–10823, 2019.
- [18] H. Li, X. Tong, Q. Li, and X. Tian. Xorlora: Lora backscatter communication with commodity devices. In *ICCC*. IEEE, 2020.
- [19] X. Li, Y. Zhang, I. Marsic, A. Sarcevic, and R. S. Burd. Deep learning for rfid-based activity recognition. In *SenSys*. ACM, 2016.
- [20] J. C. Liando, A. Gamage, A. W. Tengourtius, and M. Li. Known and unknown facts of lora: Experiences from a large-scale measurement study. *ACM Transactions on Sensor Networks (TOSN)*, 15(2):1–35, 2019.
- [21] C.-W. Liang, Y.-L. Wu, C.-Y. Shi, S.-M. Lu, and H.-C. Lee. Evaluation of a lora mesh wireless networking system supporting time-critical transmission and data lost recovery: Poster abstract. In *IPSN*. ACM/IEEE, 2019.
- [22] S. Opipah, H. Qodim, D. Miharja, Sarbini, E. A. Z. Hamidi, and T. Juhana. Prototype design of smart home system base on lora. In *ICWT*. IEEE, 2020.
- [23] S. Pan, T. Yu, M. Mirshekari, J. Fagert, A. Bonde, O. J. Mengshoel, H. Y. Noh, and P. Zhang. Footprintid: Indoor pedestrian identification through ambient structural vibration sensing. *Proceedings of the ACM on Interactive, Mobile, Wearable and Ubiquitous Technologies*, 1(3):1–31, 2017.
- [24] Y. Peng, L. Shangguan, Y. Hu, Y. Qian, X. Lin, X. Chen, D. Fang, and K. Jamieson. Plora: A passive long-range data network from ambient lora transmissions. In *SIGCOMM*. ACM, 2018.
- [25] J. Shi, D. Mu, and M. Sha. Lorabee: Cross-technology communication from lora to zigbee via payload encoding. In *ICNP*. IEEE, 2019.
- [26] Y. Shu, C. Bo, G. Shen, C. Zhao, L. Li, and F. Zhao. Magicol: Indoor localization using pervasive magnetic field and opportunistic wifi sensing. *IEEE Journal on Selected Areas in Communications*, 33(7):1443–1457, 2015.
- [27] Y. Shu, Y. Huang, J. Zhang, P. Coué, P. Cheng, J. Chen, and K. G. Shin. Gradient-based fingerprinting for indoor localization and tracking. *IEEE Transactions on Industrial Electronics*, 63(4):2424–2433, 2015.
- [28] J. R. Smith, K. P. Fishkin, B. Jiang, A. Mamishev, M. Philipose, A. D. Rea, S. Roy, and K. Sundara-Rajan. Rfid-based techniques for human-activity detection. *Communications of the ACM*, 48(9):39–44, 2005.
- [29] K. Sun, T. Zhao, W. Wang, and L. Xie. Vskin: Sensing touch gestures on surfaces of mobile devices using acoustic signals. In *MobiCom*. ACM, 2018.
- [30] V. Talla, M. Hessar, B. Kellogg, A. Najafi, J. R. Smith, and S. Gollakota. Lora backscatter: Enabling the vision of ubiquitous connectivity. *Proceedings of the ACM on Interactive, Mobile, Wearable and Ubiquitous Technologies*, 1(3):1–24, 2017.
- [31] S. Tong, J. Wang, and Y. Liu. Combating packet collisions using non-stationary signal scaling in lpwans. In *MobiSys*. ACM, 2020.
- [32] M. Uddin, A. Saleem, I. Nam, and T. Nadeem. Wearable sensing framework for human activity monitoring. In *WearSys*. ACM, 2015.
- [33] A. Varshney, O. Harms, C. Pérez-Penichet, C. Rohner, F. Hermans, and T. Voigt. Loreal: A backscatter architecture that achieves a long communication range. In *SenSys*. ACM, 2017.
- [34] C. Wang, J. Liu, Y. Chen, H. Liu, L. Xie, W. Wang, B. He, and S. Lu. Multi-touch in the air: Device-free finger tracking and gesture recognition via cots rfid. In *INFOCOM*. IEEE, 2018.
- [35] J. Wang, L. Chang, S. Aggarwal, O. Abari, and S. Keshav. Soil moisture sensing with commodity rfid systems. In *MobiSys*. ACM, 2020.
- [36] X. Wang, L. Kong, L. He, and G. Chen. mlora: A multi-packet reception protocol in lora networks. In *ICNP*. IEEE, 2019.
- [37] Y. Wang, J. Shen, and Y. Zheng. Push the limit of acoustic gesture recognition. *IEEE Transactions on Mobile Computing*, 2020.
- [38] Z. Wang, Z. Jiang, J. Hu, T. Song, and Z. Cao. Research on agricultural environment information collection system based on lora. In *ICCC*. IEEE, 2018.
- [39] C. Wu, F. Zhang, Y. Fan, and K. R. Liu. Rf-based inertial measurement. In *Proceedings of the ACM Special Interest Group on Data Communication*, pages 117–129, 2019.
- [40] X. Xia, Y. Zheng, and T. Gu. Ftrack: Parallel decoding for lora transmissions. *IEEE/ACM Transactions on Networking*, 28(6):2573–2586, 2020.
- [41] B. Xie and J. Xiong. Combating interference for long range lora sensing. In *SenSys*. ACM, 2020.
- [42] B. Xie, J. Xiong, X. Chen, and D. Fang. Exploring commodity rfid for contactless sub-millimeter vibration sensing. In *SenSys*. ACM, 2020.
- [43] Y. Xie, J. Xiong, M. Li, and K. Jamieson. md-track: Leveraging multidimensionality for passive indoor wi-fi tracking. In *MobiCom*. ACM, 2019.
- [44] X. Xu, Y. Shen, J. Yang, C. Xu, G. Shen, G. Chen, and Y. Ni. Passivelc: Enabling practical visible light backscatter communication for battery-free iot applications. In *MobiCom*. ACM, 2017.
- [45] L. Yang, Y. Li, Q. Lin, X.-Y. Li, and Y. Liu. Making sense of mechanical vibration period with sub-millisecond accuracy using backscatter signals. In *MobiCom*. ACM, 2016.
- [46] Y. Zeng, D. Wu, J. Xiong, E. Yi, R. Gao, and D. Zhang. Farsense: Pushing the range limit of wifi-based respiration sensing with csi ratio of two antennas. *Proceedings of the ACM on Interactive, Mobile, Wearable and Ubiquitous Technologies*, 3(3):1–26, 2019.
- [47] D. Zhang, J. Wang, J. Jang, J. Zhang, and S. Kumar. On the feasibility of wi-fi based material sensing. In *MobiCom*. ACM, 2019.
- [48] F. Zhang, Z. Chang, K. Niu, J. Xiong, B. Jin, Q. Lv, and D. Zhang. Exploring lora for long-range through-wall sensing. *Proceedings of the ACM on Interactive, Mobile, Wearable and Ubiquitous Technologies*, 4(2):1–27, 2020.